Numerical investigations of flow over wavy cylinders at sub-critical Reynolds number

M.R. Lekkala [a], L. Mohamed [a], J.H. Jung [b], C.K. Jin [c], B. Li [d], B. Jeong [e] and D.K. Kim [f, g] *

[a] Department of Civil and Environmental Engineering, Universiti Teknologi PETRONAS, Seri Iskandar, Perak, Malaysia

[b] Korea Research Institute of Ships and Ocean Engineering, Busan, Korea

[c] Department of Ocean Engineering, Texas A&M University, College Station, Texas, USA

[d] Shenzhen International Graduate School, Tsinghua University, Shenzhen, China

[e] Department of Naval Architecture, Ocean and Marine Engineering, University of Strathclyde, Glasgow, UK

[f] Department of Naval Architecture and Ocean Engineering, Seoul National University, Seoul, Korea

[g] Institute of Engineering Research & Research Institute of Marine Systems Engineering, Seoul National University, Seoul, Korea

Abstract

This paper presented the numerical study of three-dimensional unsteady flow behind the double wavy (DW), singe wavy (SW), and smooth circular (SC) cylinders geometry at subcritical Reynolds number ($\mathrm{Re} = 3.0 \times 10^3$) using large-eddy simulations based on the finite volume method. This study contributes to the understanding of the effects of geometric disturbances as a passive flow control method to reduce the hydrodynamic forces exerted by the fluid flow on the cylinders. The DW and SW cylinders with spanwise wavelength ratios as $\lambda/D_m = 3.79 - 6.82$ and with fixed wave amplitude ratio as $a/D_m = 0.152$ are investigated and compared with SC cylinder in terms of flow variables such as drag, lift coefficients, Strouhal number, vortex formation length, and vorticity contours of the cylinders. Furthermore, an investigation was also carried out to quantify the differences in the fluid flow properties behind SC and SW cylinders compared to DW cylinders. When compared to the SC and SW cylinders, the findings indicated that the DW cylinder reduces drag and lift coefficients significantly for every λ/D_m. A maximum reduction in fluid forces is observed at $\lambda/D_m = 6.06$ for DW cylinder; 16.63% and 94.99% reduction in mean drag and lift fluctuations respectively compared to SC cylinder. The DW cylinder also showed a longer vortex formation length than SC and SW cylinders for every λ/D_m. The flow separation angle and mean streamwise velocity distributions are also investigated and compared between the SC, SW, and DW cylinders. The present

Corresponding author: Do Kyun Kim (do.kim@snu.ac.kr)

This is a peer reviewed, accepted author manuscript of the following research article: Lekkala, M. R., Mohamed, L., Jung, J. H., Jin, C. K., Li, B., Jeong, B., & Kim, D. K. (2023). Numerical investigations of flow over wavy cylinders at sub-critical Reynolds number. Ocean Engineering, 269, [113501]. https://doi.org/10.1016/j.oceaneng.2022.113501

study reveals that the geometric surface waviness of the cylinder can be used to minimize force coefficients at a sub-critical flow regime. The obtained conclusions could provide some references to the engineering field for the design stage of slender marine structures.

Keywords: flow-induced vibrations, passive flow control method, large-eddy simulations, flow characteristics, wavy cylinders, force reduction.

1. Introduction

The flow across bluff bodies is considered as a prominent fundamental and enduring problem in fluid dynamics and has attracted the interest of many researchers in various scientific and engineering practices. Conventional bluff bodies such as smooth circular, elliptical, and square cylinders play a vital role in various fields such as the construction of high-rise buildings, chimney stacks, cable bridges, and offshore structures such as subsea risers and pipelines. These structures are exposed to unsteady flow conditions which leads to complex flow phenomena such as flow separation, vortex dynamics, flow-induced vibrations (FIV), and shear layer interactions.

Different methods are investigated in the literature in order to control wake dynamics behind the cylinders with the main objective of decreasing the magnitude of drag coefficient and lift fluctuations. Choi et al. (2008) categorized the flow around bluff bodies into boundary layer control methods (passive flow control method) and direct wake modifications methods (active flow control methods). The geometric modification method is one of the passive flow control methods proved to effectively reduce the fluid forces acting on bluff bodies (Choi et al., 2008 and Bearman and Branković, 2004). Bluff bodies experience vortex shedding beyond the critical Reynolds number (Re) resulting in unsteady hydrodynamic forces such as drag or lift force which subsequently causes the structural oscillations known as vortex-induced vibrations (VIV). Extensive studies have been carried out to develop VIV control methods such as modifying the surface of a cylinder geometry by adding helical strakes, fairings, and hemispherical bumps to the surface or by adding the buoyancy modules to the cylinder (Owen et al., 2001, Naudascher and Rockwell 2005, Assi et al., 2009, Zhou et al., 2011, Jie and Liu (2017), Sohankar et al., 2019, Zheng et al., 2021, Lekkala et al., 2022). Based on the geometry surface modification method, the smooth circular (SC) cylinder surface is modified as a symmetric sinusoidal wave along the spanwise direction called as a sinusoidal wavy cylinder, and hereafter in this study will be referred to as a symmetric wavy cylinder (SW).

Owen et al. (2001) investigated the passive flow control methods through experiments with a circular cylinder, a cylinder with a sinusoidal axis, and hemispherical bumps attached to the cylinder for Re up to 10^5. The authors observed that the cylinders with sinuous axis and hemispherical bumps have reduced drag coefficient by 47% and 25% respectively and also suppressed the vortex shedding. Lam et al. (2004a) conducted experiments to investigate the effect of the surface waviness of the cylinder on hydrodynamic coefficients and Strouhal number (St) for $Re = 2.0\times10^4$ to $5.0.0\times10^4$. The authors have reported that SW cylinders reduced the drag by 20% (depending upon the obliqueness of the cylinder) when compared with SC cylinders due to the higher base pressure caused by the waviness of the cylinder. The Strouhal number of the SW cylinder was about 0.20 for $Re = 1.0\times10^4$ to $6.0.0\times10^4$, which was identical to an SC cylinder. Lam et al. (2004b) reported that the vortex formation length of the SW cylinder is longer than the SC cylinder which resulted in the reduction of drag coefficient and suppression of vibrations. Particle Image Velocimetry (PIV) measurements at $Re = 3.0\times10^3$ were carried out by Zhang et al. (2005) to investigate the near-wake formations behind the sinusoidal cylinder. The authors have concluded that the existence of surface waviness due to the sinusoidal surface geometry considerably altered the near-wake structures, and vortices in the streamwise direction, and controls the 3D vortices formed behind the cylinder. Kravchenko and Moin (2000) conducted numerical simulation using LES with high-order B-splines at $Re = 3.9\times10^3$. The authors found that the results using B-splines are in better agreement with hot-wire experiment than results from finite-difference simulations.

Experiments were carried out by Lee and Nguyen (2007) to investigate the drag force, mean velocity profiles, and turbulent intensity behind the SW cylinder with two wavelengths ($\lambda = 1D$ and $2D$) for $Re = 5.0\times10^3$ to 2.0×10^4. At $Re = 1.0\times10^4$, the SW cylinder reduced the drag coefficient by 22% compared to the SC cylinder, and periodic wake structures were observed along the spanwise direction. They concluded that the vortex formation length of the SW cylinder is larger than the SC cylinder which suppressed the drag coefficient. These results were in good agreement with the observations of Lam et al. (2004b). Ahn et al. (2009) considered three separate wavelengths ($\lambda = \pi/2, \pi/3,$ and $\pi/4$) with constant wavy amplitude as 0.1 and Prandtl number (Pr)=0.71 to study the effect of waviness on the heat transfer at $Re = 300$. They found that the larger time- and local surface-average Nusselt number ($\langle\langle\overline{Nu}\rangle\rangle$) at nodes when compared to the saddle location of the SW cylinder. The $\langle\langle\overline{Nu}\rangle\rangle$ value at $\lambda = \pi/2$ is greater than the SC cylinder, whereas at $\lambda = \pi/3$ and $\pi/4$,

values are smaller than that of the SC cylinder. It was concluded that the variation of $\langle\langle\overline{Nu}\rangle\rangle$ for SW cylinders strongly depended on the location of a point in the spanwise direction and wavelength.

An experimental study was carried out by New et al. (2013) to investigate the effect of λ/D_m and a/D_m on the SW cylinder at $Re = 2.7\times10^3$ using PIV measurement. The authors have summarized that smaller wavelength cylinders are less sensitive to aspect ratios (AR) and end conditions of the geometry due to the vortices in a streamwise direction at nodes and saddle points. Recently, Assi and Bearman (2018) carried out experiments to investigate the VIV of SW cylinders in water channels for $Re = 1.5\times10^3$ to 1.5×10^4. They revealed that the wavy surface of the cylinder affects the vortex formation in the wake by producing streamwise and crossflow vortices and the SW cylinder has reduced C_D by 12.5% compared to the SC cylinder. Bai et al. (2019) investigated the flow behind symmetric wavy cylinders with three different wavelengths and concluded that $\lambda/D_m = 1.89$ and 6.06 produced significantly larger streamwise vortices than $\lambda/D_m = 3.79$. Zhang et al. (2018) studied the flow behind the oscillating wavy cylinder subjected to forced vibrations at $Re = 5.0\times10^3$. The authors have found that the drag and lift coefficients of the wavy cylinder are similar to the smooth circular cylinder. They have also concluded that vortex shedding patterns resemble to smooth circular cylinders.

Lam and Lin (2008) carried out large-eddy simulations (LES) studies on SW cylinders with $\lambda/D_m = 1.14 - 3.33$ at $Re = 3.0\times10^3$. At this Re, the maximal C_D reduction was up to 18% compared with an SC cylinder at optimal $\lambda/D_m = 1.9$ and $a/D_m = 0.152$. Furthermore, the authors discovered that wave amplitude to wavelength ratio (a/λ) plays a vital role in identifying the structure of the vortex formations past the SW cylinder and also has a significant impact on the suppression of flow-induced vibrations (FIV). Lam and Lin (2009) considered a wide range of λ/D_m from 1.0 to 10.0 and a/D_m from 0.02 to 0.30 at $Re = 100$. At this Re and optimal $\lambda/D_m = 6.0$, the drag and lift coefficients of the SW cylinder decreased sharply as a/D_m increased. The maximum reduction in drag that was achieved was up to 18% and the lift coefficient was almost zero which indicates that SW cylinders are ideal to suppress FIV. Additionally, the authors have stated that the optimal value of λ/D_m depends on Re in laminar flow regime. While Lin et al. (2016) continued the study carried out by Lam and Lin (2008) with λ/D_m from 3.79 to 7.57 and constant $a/D_m = 0.152$ using 3D LES at $Re = 3.0\times10^3$. The authors identified three different regimes based on λ/D_m and wake formations namely: regime I, II, and III at

$\lambda/D_m < 6.0, = 6.0$ and > 6.0 respectively. At optimal $\lambda/D_m = 6.06$, the SW cylinder reduced the drag and lift coefficients by 16% and 93% respectively compared to the SC cylinder. Xu et al. (2010) carried out numerical simulations using LES at $Re = 2.0x10^5$ to investigate the flow behind the SW cylinder. They determined that the waviness of the cylinder as a passive flow control method reduced the drag by up to 26% while the lift coefficient was suppressed to zero in comparison with a SC cylinder. The authors have found that the shear-layer shed from the SW cylinder was steadier than the SC cylinder which delayed the vortex rolling that led to higher base pressure. They have concluded that the greater base pressure of the SW cylinder was primarily responsible for the reduction in the drag coefficient. Jung and Yoon (2014) developed a helically twisted elliptic cylinder (HTE) by twisting the elliptical cylinder along its spanwise direction. The authors have investigated the flow characteristics of HTE, SW, and SC cylinders and concluded that HTE reduced the drag coefficient by 13% and 5% when compared to SW and SC cylinders respectively and the root mean square (RMS) lift coefficient was reduced by 96% compared to the SC cylinder at $Re = 3.0 \times 10^3$. Zhuang et al. (2018) investigated the unsteady flow behind a rotating SW cylinder at $Re = 3.8 \times 10^3$. The authors have stated that as the rotation rate increases, the formation length of the vortices increases which supports suppressing of the von-Karman vortex shedding. They have observed that, in order to achieve the mean lift force similar to a rotating circular cylinder, the rotational rate for an SW cylinder should be twice that of an SC cylinder. Yoon et al. (2020) investigated the effect of double wavy (DW) disturbance of the cylinder on drag and lift coefficients at $Re = 3.0 \times 10^3$ with $\lambda/D_m = 6.06$. The authors have concluded that the DW cylinder reduces the drag and lift coefficient by 16.74% and 97.27% respectively when compared to the SC cylinder. Nam and Yoon (2022) have explored the influence of wavy disturbances on the flow around an elliptic cylinder at for various aspect ratios at $Re = 100$. The authors have classified the flow into three modes namely: (I) steady, (II) Unsteady, and (III) coexistence states based on a bifurcation map. Dong et al. (2006) investigated the development of shear layer instabilities using PIV and numerical simulations at $Re = 3.9 \times 10^3$, 4.0×10^3, and 10×10^3. The authors have found that at high Re the length of the shear layer and wake bubble decrease significantly.

To the authors' knowledge, the only previous research on DW cylinder was carried out by Yoon et al. (2020) with $\lambda/D_m = 6.06$ at $Re = 3.0 \times 10^3$. The main objective of the present study is to assess the potential of the DW cylinder as a passive flow control method to investigate the flow features to present the optimal wavelength. In this study, five different λ/D_m (3.79, 4.55, 5.30, 6.06, and 6.82)

with a fixed $a/D_m = 0.152$ are considered to study the effect of double waviness on the time variation and mean values of drag and lift coefficients at $Re = 3.0\times10^3$. The present study considered large-eddy simulations (LES) to solve momentum and energy equations that regulate the flow around SC, SW, and DW cylinders in turbulent flow regimes. Eventually, comparisons were made between the SC, SW, and DW cylinders in order to view the effects of waviness along the spanwise direction. Therefore, the flow around different geometries (SC, SW, DW) for different λ/D_m and fixed a/D_m are numerically simulated and analyzed. The computational details, numerical aspects, and cylinder details are described in section 2. In section 3, results and discussions are presented and finally, conclusions and further recommendations are summarized in section 4.

2. Computational details

2.1 Governing Equations and Sub-Grid Scale model

The present study considered 3D unsteady incompressible Navier-Stokes equations as governing equations to solve the incompressible viscous flow across the cylinders. A subcritical flow regime at the Reynolds number $Re = 3.0\times10^3$ considered in the present study for flow across the circular cylinder. The governing grid filtered Navier-Stokes and continuity equations employed in LES are defined as follows:

$$\frac{\partial \overline{u_i}}{\partial t} + \frac{\partial \overline{u_i u_j}}{\partial x_j} = -\frac{\partial \overline{p}}{\partial x_i} + \frac{1}{Re}\frac{\partial^2 \overline{u_i}}{\partial x_j \partial x_j} - \frac{\partial \tau_{ij}}{\partial x_j}, \qquad (i = 1, 2, 3) \tag{1}$$

$$\frac{\partial \overline{u_i}}{\partial x_i} = 0 \tag{2}$$

where $\overline{u_i}$ are the filtered velocity components in cartesian coordinates x_i, t and p are time and pressure respectively. τ_{ij} is the sub-grid scale stress tensor defined as $\tau_{ij} = \overline{u_i u_j} - \overline{u_i}\,\overline{u_j}$ and represents the impact of the sub-grid scales on large scales that result from the filtering operation, which are undetermined and have to be modeled from the sub-grid model. The eddy-viscosity model is used in the sub-grid scale (SGS) model, and the anisotropic component of the SGS model stress tensor assumes the following form:

$$\tau_{ij}^a = \tau_{ij} - \frac{1}{3}\tau_{kk}\delta_{ij} = -2\nu_T \overline{S_{ij}} \tag{3}$$

Smagorinsky (1993) proposed the most extensively used eddy-viscosity model as follows:

$$\nu_T = (C_S \Delta)^2 \left|\bar{S}\right| \tag{4}$$

where filter width $\Delta = (\Delta_1, \Delta_2, \Delta_3)^{1/3}$ (Deadroff, 1970), where $\Delta_1, \Delta_2,$ and Δ_3 are the sizes of the computational cells, $\left|\bar{S}\right| = (2\overline{S_{ij}}\,\overline{S_{ij}})^{1/2}$ with $\overline{S_{ij}} = ((\partial \overline{u_i}/\partial x_j) + (\partial \overline{u_j}/\partial x_i))/2$ and C_S is the Smagorinsky constant.

The present study adopts the dynamic Smagorinsky (SGS) model proposed by Germano et al. (1991) to represent the unresolved sub-grid scale fluid motion. The second filter is set and then applied to the large eddy as defined in Eq. (1):

$$T_{ij} = \overline{u_i u_j} - \bar{u}_i \bar{u}_j \tag{5}$$

$$L_{ij} = \overline{u_i}\,\overline{u_j} - \bar{u}_{ij} \bar{u}_j \tag{6}$$

Germano identity is used to characterize the stresses:

$$L_{ij}^a = T_{ij}^a - \tilde{\tau}_{ij}^a \tag{7}$$

where

$$T_{ij}^a = -2(C_S \tilde{\Delta})^2 |\bar{S}| \bar{S}_{ij} \tag{8}$$

Here $\tilde{\Delta}$ is defined as the characteristic filter width that is related to the test filter. Finally, the following equation yields a space- and time-dependent Smagorinsky coefficient:

$$(C_s \Delta)^2 M_{ij} = L_{ij}^a \tag{9}$$

$$\text{where } M_{ij} = -2\left(\frac{\tilde{\Delta}}{\Delta}\right)^2 |\bar{S}| \bar{S} + 2|\bar{S}|\bar{S}_{ij} \tag{10}$$

More details of the present SGS model can be found in Yoon et al. (2009) and Jung and Yoon (2014). Jung and Yoon (2014) have successfully used the Smagorinsky SGS model to study the flow over a helically twisted cylinder at the same Re used in this study.

2.2 Numerical methodology

In present numerical investigations, the finite-volume method (FVM) is employed on structured grids to compute the solution of the 3D unsteady incompressible Navier-Stokes equations. For momentum discretization, a second-order central differencing scheme is used while a two-step time split scheme is employed for temporal discretization, and a Poisson equation is solved to meet

the continuity condition. For diffusive and convective terms, the Crank-Nicolson scheme and second-order Adams-Bashforth scheme are employed, respectively. A well-known Pressure-Implicit with Splitting of Operators (PISO) algorithm is used for pressure-velocity coupling between momentum and the continuity equations. This numerical methodology was successfully used by Jung and Yoon (2014).

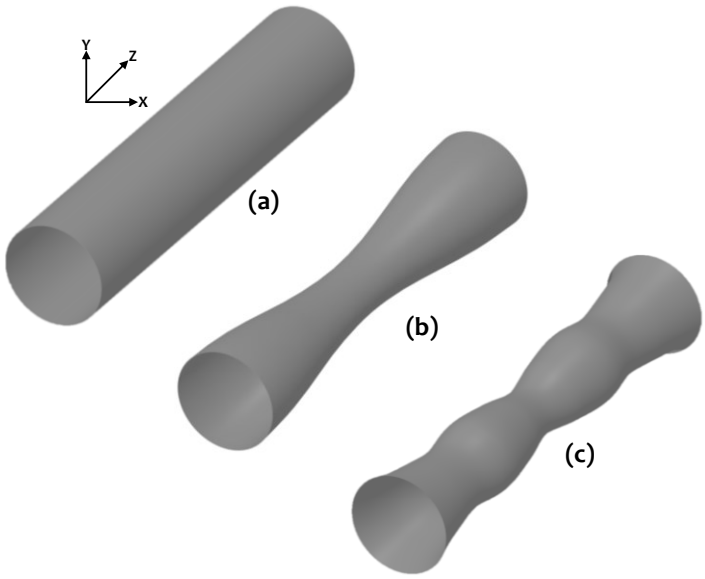

Fig. 1. The geometry of the cylinders (a) smooth circular (SC), (b) symmetric wavy (SW), and (c) double wavy (DW) cylinders.

2.3 Computational domain and boundary conditions

The different shapes of the smooth circular (SC), symmetric wavy (SW), and double wavy (DW) cylinders used in this study are shown in Fig. 1. The local diameter (D_z) of the SW cylinder is determined as follows:

$$D_z = D_m + 2a\cos\left(\frac{2\pi z}{\lambda_1}\right) \tag{11}$$

Where 'a' and λ_1 are amplitude and wavelength, respectively. D_m designate mean diameter of maximum and minimum diameters of the cylinder (D_{max} and D_{min}). It is noteworthy that D_m of the SW and DW cylinders and the diameter of the SC cylinder are the same in this study. The notations S(saddle), M(middle), and N(Node) correspond to the local diameters D_{min} , D_m , and D_{max} respectively as shown in Fig. 2. The effect of wavelength amplitudes was examined by Lam and Lin (2008), and

noticed a greater effect at $a/D_m = 0.152$ for square cylinders, therefore $a/D_m = 0.152$ is adopted in the present study to examine the effect of wavelength on SC, SW, and DW cylinders. Flow around a SC cylinder with D_m is considered as a baseline for comparison purposes.

The geometry of the DW cylinder as shown in Fig. 2 is defined as follows with two different wavelengths as follows:

$$D_Z = D_m + a\left[\cos\left(\frac{2\pi z}{\lambda_1}\right) + \cos\left(\frac{2\pi z}{\lambda_2}\right)\right] \tag{12}$$

here λ_2 is taken as $\lambda_1/3$ of the SW cylinder. As illustrated in Fig. 2 (c), the DW cylinder contains two nodes and two saddle points in the half-wavelength, in total four-node and four saddle points along the spanwise direction of the cylinder.

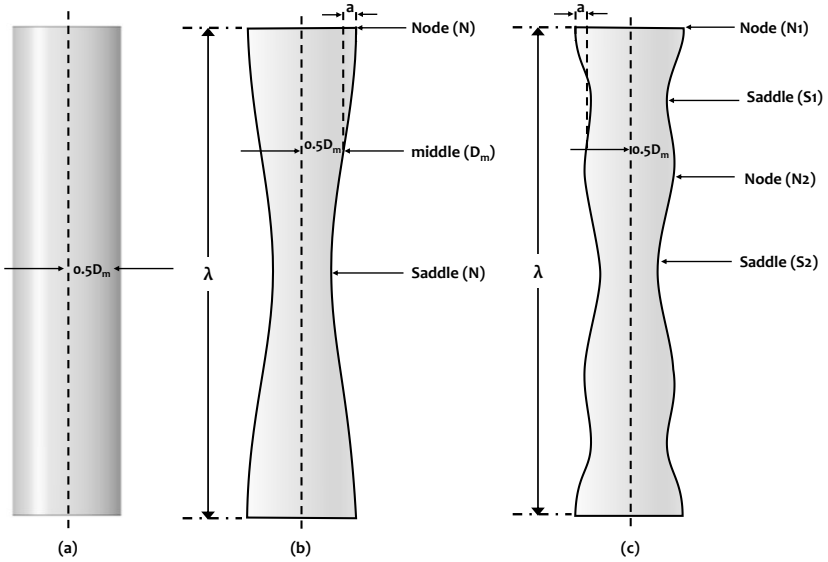

Fig. 2. Definition of cylindrical geometries used in this study (a) SC (b) SW (c) DW cylinders.

Fig. 3 presents the details of the computational domain and boundary conditions used in the present study. As shown in Fig. 3, the present study used an O-type grid with far-field limitations at a distance of $20D_m$ from the cylinder's center in the x-y plane. The cylinder models with spanwise length and details of the grid size are presented in Table 1. A uniform flow velocity is defined at the inlet boundary and at the outlet boundary, and a convective boundary condition is defined as follows: $(\partial u_i/\partial t) + (c\partial u_i/\partial x) = 0$ where 'c' is the space-averaged streamwise outlet velocity. In the outlet region, a Neuman boundary condition is used for the pressure outlet. No-slip and no-penetration boundary conditions were used for the cylinder surface.

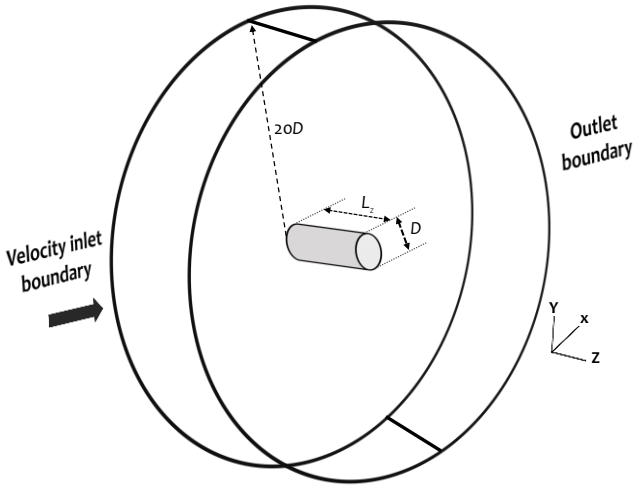

Fig. 3. The details of the computational domain and enforced boundary conditions were used in this study.

Table 1. Details of the cylinder models with wavelength and amplitude ratios, mesh, and domain sizes.

Model	λ/D_m	a/D_m	$N_r \times N_\theta \times N_z$	Domain size
1	3.79	0.152	268x222x70	20x20x3.79
2	4.55	0.152	268x222x82	20x20x4.55
3	5.30	0.152	268x222x94	20x20x5.30
4	6.06	0.152	268x222x106	20x20x6.06
5	6.82	0.152	268x222x118	20x20x6.82

2.4 Grid dependence and validation study

The grid dependence is carried out for SC, and SW cylinder cases. To find the optimal grid, the numerical results are compared and analyzed with three different mesh sizes as presented in Table 2. The non-dimensional time step is defined as $U\Delta t/D = 0.001$ meeting the CFL<1.0 throughout the simulations, where CFL is Courant-Friedrichs-Lewy $= U\Delta t/\Delta x$. The value of $y^+ = u^* \Delta y_1/\nu$ is always smaller than 1.0 in all simulations, where y_1 and u^* grid-scale of the boundary layer and friction velocity near the wall. To validate the present numerical methodology and grid size, the results are presented in terms of mean drag coefficient ($\overline{C}_D$), root mean square (RMS) of lift coefficient ($C_{L,RMS}$), and Strouhal number (St) and are compared with the results available in the literature. In this study, the drag coefficient (C_D), lift coefficient (C_L), and pressure coefficients (C_P) are defined as follows:

$$C_D = \frac{2F_D}{\rho U_\infty^2 D_m L} \tag{13}$$

$$C_L = \frac{2F_L}{\rho U_\infty^2 D_m L} \tag{14}$$

$$C_P = \frac{2(P - P_\infty)}{\rho U_\infty^2} \tag{15}$$

where F_L and F_L are total drag and lift force respectively, U_∞ and ρ are free stream velocity and density of the fluid flow respectively, D_m and L are the mean diameter and spanwise length of the cylinder respectively. P and P_∞ are static pressure on the cylinder surface at which the pressure coefficient is being evaluated and pressure in freestream, respectively. The Strouhal number (St) is a non-dimensional parameter that defines the vortex shedding frequency (F_s) and is termed as below:

$$St = \frac{F_s D_m}{U_\infty} \tag{16}$$

To validate the present numerical model and the grid, a grid dependency analysis for the SC cylinder was conducted, and the results were compared with the experimental and numerical results available from the previously published research. Three grid sizes (coarse, medium, and fine) as shown in Table 2 are considered for grid dependence analysis. The numerical model is validated in terms of time-averaged mean drag coefficient ($\bar{C}_D$), RMS of lift coefficient ($C_{L,rms}$), and Strouhal number (St). The wavelength ratio (λ / D_m) i.e., the spanwise extent of the cylinder and computational domain to validate the model is taken as 6.06 which was the optimal wavelength ratio for the SW cylinder (Lam and Lin, 2008).

Initially, the results of the flow around SC cylinder from three grid sizes are compared to the experiment by Norberg (1987) and numerical analysis by Lu et al. (1997) and LES results from Yoon et al. (2017), and Jung and Yoon (2014). Moreover, the same grid sizes are used from the SW cylinder and the results are compared with Yoon et al. (2017), Lam and Lin (2009), and Yoon et al. (2020) as presented in Table 2. Hereafter, all the inquiries presented will be based on the fine mesh, which primarily takes into account the simulation time and the accuracy of the results. The results from the flow around SC and SW cylinders agreed well with published experimental and numerical studies. The blockage ratio (B) is 5% for the SC and wavy cylinders based on the mean diameter of the cylinders. The maximum turbulence intensity observed for SC cylinder is 1.92% which is consistent with Lam et al. (2004b) and Jung and Yoon (2014). Furthermore, by using the fine grid, the mean streamwise velocity ($\bar{u}/U_\infty$) and RMS streamwise velocity (u'/U_∞) at different points along the computational domain for

SC cylinder are compared and these results showed good agreement with published experimental and numerical results as illustrated in Fig. 4.

Table 2. Grid dependency test for the SC and SW cylinder with $\lambda/D_m = 6.06$ at $Re = 3.0\times10^3$ comparison with experimental and numerical simulation results.

Geometry	Case	$N_r \times N_\theta \times N_z$	$\bar{C}_D$	$C_{L,rms}$	St
SC	Coarse	240 x 198 x 94	1.0284	0.1247	0.201
	Medium	252 x 210 x 106	1.0292	0.1274	0.211
	Fine	268 x 224 x 118	1.0297	0.1277	0.213
	Norberg (1987)	Experimental	0.98-1.030	---	0.210-0.213
	Lu et al., 1997	Analytical	1.020	---	----
	Yoon et al., 2017	23664 x 148	1.0229	0.1650	0.210
	Yoon et al., 2020	29640 x 120	1.0287	0.1296	0.210
SW	Coarse	240 x 198 x 94	0.8824	0.0185	0.181
	Medium	252 x 210 x 106	0.8855	0.0184	0.182
	Fine	268 x 224 x 118	0.8908	0.0186	0.182
	Yoon et al., 2017	23664 x 148	0.8926	0.0148	0.180
	Lin et al., 2016	16000 x 100	0.9040	0.0130	0.187
	Yoon et al., 2020	29640 x 120	0.8748	0.0101	0.180

The flow across the DW cylinder was only studied by Yoon et al. (2020) with $\lambda/D_m = 6.06$ and $a/D_m = 0.152$ at $Re = 3.0\times10^3$. To validate our numerical model with the available DW cylinder data, a grid dependence study was carried out as presented in Table 3.

Table 3. Grid dependence analysis for DW cylinder with $\lambda/D_m = 6.06$ at $Re = 3.0\times10^3$.

Case	$N_r \times N_\theta \times N_z$	$\bar{C}_D$	$C_{L,RMS}$	St
Coarse	240 x 212 x 94	0.8547	0.0066	0.180
Medium	252 x 224 x 106	0.8492	0.0064	0.181
Fine	268 x 236 x 118	0.8585	0.0068	0.179
Yoon et al., 2020	LES	0.8615	0.0040	0.180

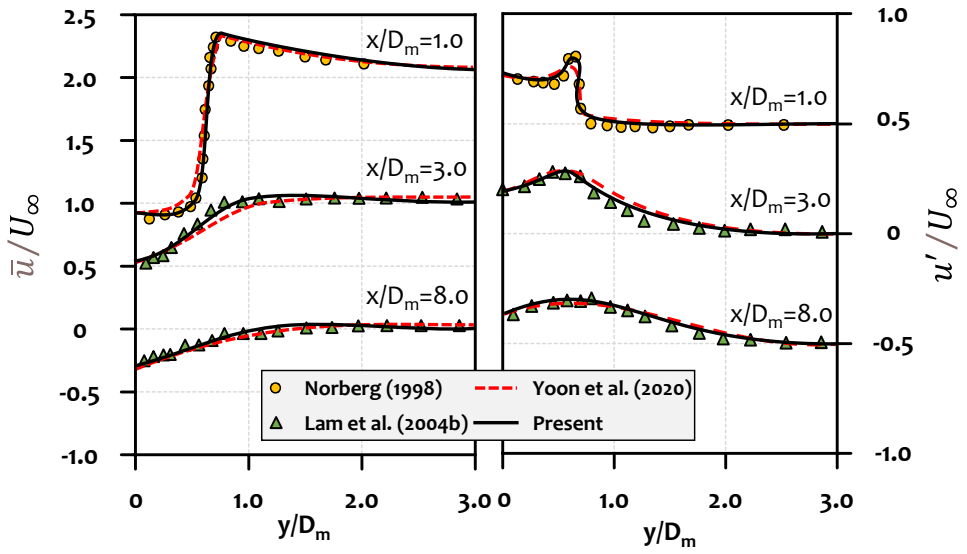

Fig. 4. Comparison of present LES turbulence model results in terms of mean streamwise velocity ($\bar{u}/U_\infty$) (left) and RMS streamwise velocity (u'/U_∞) (right) along the streamwise length of the SC cylinder at different positions at $Re = 3.0 \times 10^3$ with experimental and numerical results.

3. Results and Discussions

3.1 Drag, lift coefficients, and Strouhal number

The primary objective of flow control is to mainly reduce the drag (C_D) and lift (C_L) coefficients. Thus, the variation of C_D and C_L for SC, SW, and DW cylinders are presented in Figs. 5 and 6 as a function of time. The C_D and C_L of the SW cylinder are of lower value compared to the SC cylinder as shown in Figs. 5 and 6, which agrees well with Lin et al. (2016) for $\lambda/D_m = 6.06$. Furthermore, the DW cylinder reduced the C_D and C_L compared to SC and SW cylinders. The mean drag coefficient ($\bar{C}_D$) and root mean squared (RMS) of lift coefficient ($C_{L,RMS}$) are presented in Table 4. It can be observed that the SW cylinder was reduced $\bar{C}_D$ and $C_{L,RMS}$ by 13.49% and 85.43% respectively compared to a SC cylinder. When $\bar{C}_D$ for DW cylinders are compared to SC and SW cylinders, a reduction of 3.63% and 16.63% respectively is obtained. In addition, for $C_{L,RMS}$ reductions of 94.99% and 65.59% are obtained when compared to SC and SW cylinders, respectively for DW cylinders. Taking into account the fact that the DW cylinder significantly reduces the drag and lift forces than the SW cylinder when compared to the SC cylinder.

Table 4. Comparison of $\bar{C}_D$ and $C_{L,RMS}$ at $Re = 3.0\times10^3$ and $\lambda/D_m = 6.06$.

Cylinder	$\bar{C}_D$	% of diff.	$C_{L,RMS}$	% of diff.
SC	1.0297	---	0.1277	---
SW	0.8908	-13.49	0.0186	-85.43
DW	0.8585	-16.63	0.0068	-94.99

To estimate the Strouhal number (St) for different cylinders, Fourier transformation is applied to the time history of the C_L. The St of SC, SW, and DW cylinders are 0.213, 0.182, and 0.179 respectively. It can be inferred that the small St of the SW and DW cylinders are correlated to a longer vortex formation length (L_F) than the SC cylinder. This L_F results in the suppression of vortex shedding behind the cylinder which is discussed in later sections. These findings are consistent with studies conducted by Lin et al. (2016) and Yoon et al. (2020).

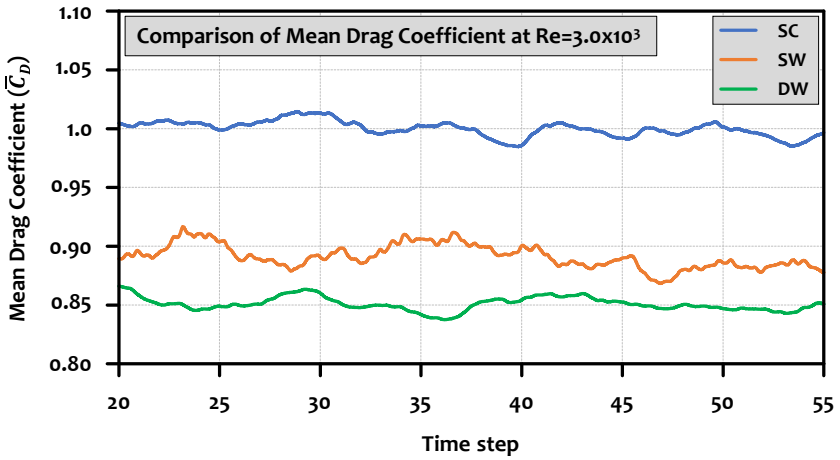

Fig. 5. Comparison of drag coefficient as a function of time for SC, SW and DW cylinders for $\lambda/D_m = 6.06$ at $Re = 3.0\times10^3$.

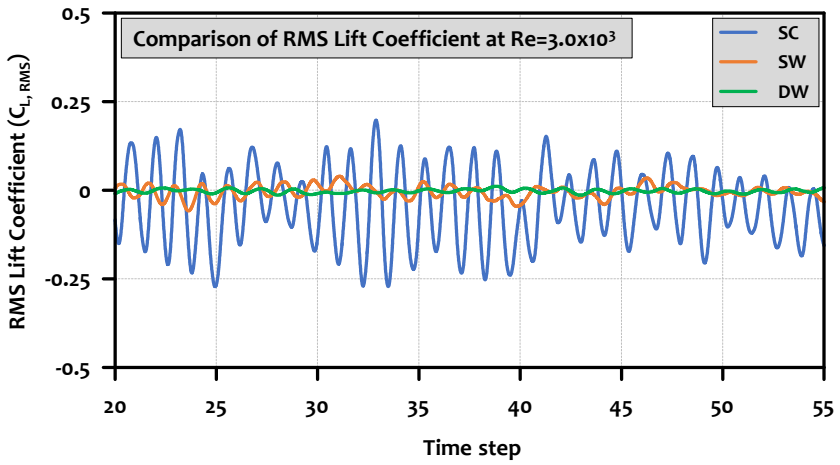

Fig. 6. Comparison of lift coefficient as a function of time for SC, SW and DW cylinders for $\lambda/D_m = 6.06$ at $Re = 3.0\times10^3$.

The variation of $\bar{C}_D$ for SW and DW cylinders with λ/D_m is presented in Fig. 7. The $\bar{C}_D$ of SC and SW cylinders as presented in Table 5 are consistent with Lin et al. (2016) using LES for $\lambda/D_m = 3.79-6.82$ at $Re = 3.0\times10^3$. From Fig. 7, it can be observed that, for SW cylinders, $\bar{C}_D$ decreases as the λ/D_m increases until $\lambda/D_m = 6.06$ and then increases for further increase in λ/D_m to 6.82 again which is in good agreement with Lin et al. (2016). An analogous trend is observed for DW cylinders. It can be observed from Table 5, that the minimum reduction in $\bar{C}_D$ for SW occurred at $\lambda/D_m = 3.79$, while the maximum reduction occurred for $\lambda/D_m = 6.06$. The optimum λ/D_m value for the SW cylinder which corresponds to the minimum value of $\bar{C}_D$ was observed at 6.06 and it agreed well with Lin et al. (2016). At this optimum λ/D_m, the SW cylinder was reduced $\bar{C}_D$ by 13.49% compared to the SC cylinder. Similarly, from Tables 6 and 7, the minimum and maximum reduction of $\bar{C}_D$ achieved by DW cylinder occurs at $\lambda/D_m = 3.79$ and $\lambda/D_m = 6.06$ respectively when compared with SW and SC cylinders. The optimum λ/D_m value for the DW cylinder occurs at 6.06 and at this optimum λ/D_m, the DW is reduced the $\bar{C}_D$ by 3.62% and 16.63% compared to SW and SC cylinders respectively.

Moreover, the $C_{L,RMS}$ decreases for SW and DW cylinders as λ/D_m increase up to 6.06 and then increases as λ/D_m increases as shown in Fig. 8. Specifically, at $\lambda/D_m = 6.06$, the SW and DW cylinders were reduced the $C_{L,RMS}$ by 86.03% and 94.90% respectively compared with the SC cylinder as presented in Tables 5 and 6. While the minimum reduction of $C_{L,RMS}$ occurred at $\lambda/D_m = 3.79$ for both

SW and DW cylinders compared to the SC cylinder which is identical behavior observed for $\bar{C}_D$. From Table 7, it can be noted that at every λ/D_m, the DW cylinder was reduced $\bar{C}_D$ and $C_{L,RMS}$ compared to SW cylinder. Finally, it can be inferred that for every λ/D_m, more reduction in $\bar{C}_D$ and $C_{L,RMS}$ can be obtained from DW cylinder than SW cylinder compared to SC cylinder at $Re = 3.0\times10^3$. By comparing the $C_{L,RMS}$ between three cylinders, the lift fluctuations on the DW cylinder are significantly suppressed. Tables 5, 6, and 7 summarize the percentage of difference in $\bar{C}_D$ and $C_{L,RMS}$ between the three cylinders. Among the different combinations in the calculation of the percentage of difference, the DW cylinder showed the highest reduction in $\bar{C}_D$ and $C_{L,RMS}$ for every λ/D_m compared with SC and SW cylinders.

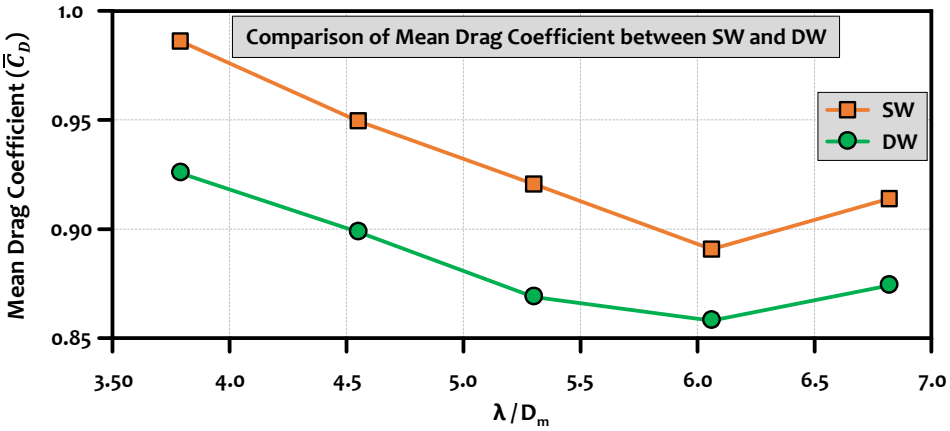

Fig. 7. Comparison of $\bar{C}_D$ between SW and SW cylinders at $Re = 3.0\times10^3$ for different λ/D_m.

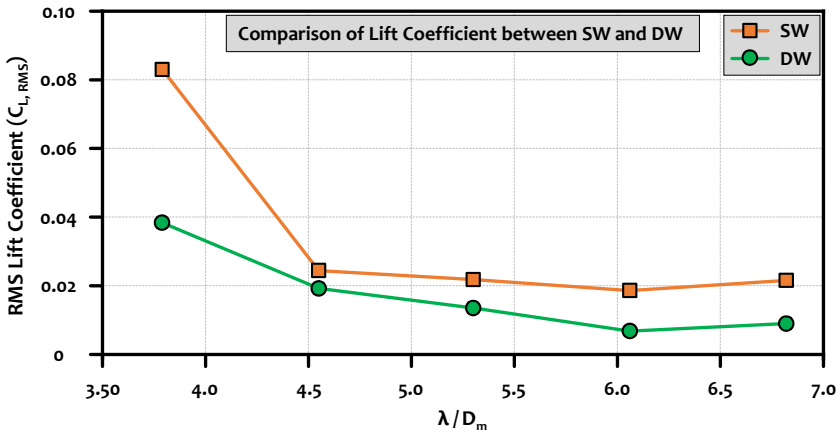

Fig. 8. Comparison of $C_{L,RMS}$ between SW and SW cylinders at $Re = 3.0\times10^3$ for different λ/D_m.

Table 5. Comparison of percentage of the difference between $\bar{C}_D$ and $C_{L,RMS}$ for SC and SW cylinders at $Re = 3.0 \times 10^3$ for different wavelength ratios.

λ / D_m	Percentage of difference between SC and SW					
	$\bar{C}_D$			$C_{L,RMS}$		
	SC	SW	e* (%)	SC	SW	e* (%)
3.79	1.0297	0.9862	-4.23	0.1332	0.0830	-37.69
4.55	1.0297	0.9497	-7.77	0.1332	0.0244	-81.66
5.30	1.0297	0.9206	-10.60	0.1332	0.0218	-83.64
6.06	1.0297	0.8908	-13.49	0.1332	0.0186	-86.03
6.82	1.0297	0.9140	-11.24	0.1332	0.0216	-83.82

$$*e = \frac{SC - SW}{SC} \times 100$$

Table 6. Comparison of percentage of the difference between $\bar{C}_D$ and $C_{L,RMS}$ for SC and DW cylinders at $Re = 3.0 \times 10^3$ for different wavelength ratios.

λ / D_m	Percentage of difference between SC and DW					
	$\bar{C}_D$			$C_{L,RMS}$		
	SC	DW	f* (%)	SC	DW	f* (%)
3.79	1.0297	0.0830	-10.06	0.1332	0.0384	-71.18
4.55	1.0297	0.0244	-12.68	0.1332	0.0192	-85.59
5.30	1.0297	0.0218	-15.58	0.1332	0.0135	-89.87
6.06	1.0297	0.0186	-16.63	0.1332	0.0068	-94.90
6.82	1.0297	0.0216	-15.06	0.1332	0.0090	-93.27

$$*f = \frac{SC - DW}{SC} \times 100$$

Table 7. Comparison of percentage of the difference between $\bar{C}_D$ and $C_{L,RMS}$ for SW and SW cylinders at $Re = 3.0 \times 10^3$ for different wavelength ratios.

λ / D_m	Percentage of difference between SW and DW					
	$\bar{C}_D$			$C_{L,RMS}$		
	SW	DW	g* (%)	SW	DW	g* (%)
3.79	0.9862	0.9261	-6.09	0.0830	0.0384	-53.75
4.55	0.9497	0.8991	-5.32	0.0244	0.0192	-21.42
5.30	0.9206	0.8693	-5.57	0.0218	0.0135	-38.09
6.06	0.8908	0.8585	-3.62	0.0186	0.0068	-63.47
6.82	0.9140	0.8746	-4.30	0.0216	0.0090	-58.40

$$*g = \frac{SW - DW}{SW} \times 100$$

Table 8 summarizes the percentage of $\bar{C}_D$ and $C_{L,RMS}$ obtained for different cross-sectional geometries of the cylinder at various Re from the literature. In this paragraph, the base cylinder is taken as the SC cylinder and the reduction in force coefficients achieved by the SW cylinder is compared with the base case unless specified. The Re ranges from laminar to subcritical flow regime covering $100 \le Re \le 5.0\times10^4$ and λ/D_m in the range of 1.0 to 10.0. Bearman and Owen (1998) attained a significant reduction in $\bar{C}_D$ (30%) at $Re = 4.0\times10^4$ for a square cylinder with a wavy front face at an optimum $\lambda/D_m = 5.60$, while Darekar and Sherwin (2001) obtained a 16% reduction in $\bar{C}_D$ with the same optimum λ/D_m as Bearman and Owen (1998) at $Re = 100$. Lam et al. (2004a) observed a smaller optimum λ/D_m (2.08) at which the $\bar{C}_D$ was reduced by 20% for Re in the range of $2.0\times10^4 - 5.0\times10^4$, whereas Lam and Lin (2008) attained 18% and 94% reduction in $\bar{C}_D$ and $C_{L,RMS}$ respectively for optimum $\lambda/D_m = 1.9$ at $Re = 3.0\times10^3$. However, Lam and Lin (2009) observed two optimal λ/D_m at $Re = 100$ where an 18% and 99% reduction in $\bar{C}_D$ and $C_{L,RMS}$ respectively was obtained for $\lambda/D_m = 2.5$ *and* 6.0. At $\lambda/D_m = 4.55$, Jung and Yoon (2014) have achieved a reduction of 8% and 78% in $\bar{C}_D$ and $C_{L,RMS}$ respectively by SW cylinder at $Re = 3.0\times10^3$ compared to SC cylinder. Lin et al. (2016) used a large range of λ/D_m at $Re = 3.0\times10^3$ and obtained a maximum reduction of 16% and 94% for $\bar{C}_D$ and $C_{L,RMS}$, respectively. At $Re = 3.0\times10^3$ with $\lambda/D_m = 6.06$, Yoon et al. (2017) and Moon et al. (2019) observed a reduction of 12.74% and 9.47% in $\bar{C}_D$ respectively, while a reduction of 91.02% and 84.06% in $C_{L,RMS}$, respectively was also obtained.

Yoon et al. (2020) obtained a reduction of 13.05% and 16.74% in $\bar{C}_D$ for SW and DW cylinders at $Re = 3.0\times10^3$ when compared to SC cylinders at $\lambda/D_m = 6.06$. For $C_{L,RMS}$, the authors have achieved a reduction of 88.26% and 97.27% for SW and DW cylinders when compared with SC cylinders. In the present investigation, an optimum λ/D_m for SW cylinder was observed at 6.06 which matches with Lin et al. (2016). Similarly, an optimum λ/D_m for DW cylinder was observed at 6.06 where the reduction in $\bar{C}_D$ and $C_{L,RMS}$ is 16.6% and 94.9% respectively when compared to SC cylinder as presented in Table 8. Subsequently, based on these experimental and numerical studies as presented in Table 8, it can be concluded that the optimum λ/D_m is less influenced by the waviness of the cross-section of the

cylinder and Re, the maximum reduction in force coefficients occurs around either at $\lambda/D_m \approx 2.0$ or 6.0.

Table 8. Comparison of percentage of $\overline{C}_D$ reduction achieved by other researchers in the literature.

Researcher	Type of Cylinder	Re	Range of λ/D_m	Optimal λ/D_m	% of $\overline{C}_D$ reduction achieved	% of $C_{L,RMS}$ reduction achieved
Darekar and Sherwin, 2001	Square	100	1.0-10.0	5.6	16	----
Bearman and Owen, 1998	Square	4.0×10^4	3.5-5.6	5.6	30	----
Lam et al., 2004a	SW	$2.0\times10^4 - 5.0\times10^4$	1.45-2.27	2.08	20	----
Lam and Lin, 2008	SW	3.0×10^3	1.136-3.333	1.9	18	94
Lam and Lin, 2009	SW	100	1.0-10.0	2.5, 6.0	18	99
Jung and Yoon, 2014	SW	3.0×10^3	4.55	----	8	78
Lin et al., 2016	SW	3.0×10^3	3.79-7.57	6.06	16	94
Yoon et al., 2017	SW	3.0×10^3	6.06	6.06	12.74	91.02
Moon et al., 2019	SW	3.0×10^3	6.06	6.06	9.47	84.06
Yoon et al., 2020	SW	3.0×10^3	6.06	6.06	13.05	88.26
	DW				16.74	97.27
Present	SW	3.0×10^3	3.79-6.82	6.06	13.49	86.03
	DW			6.06	16.60	94.9

The reduction in C_D and suppression of C_L by the wavy (Lin et al.2016), helical (Yoon et al., 2018), and spiral (Xu et al., 2019) types of geometric disturbances are generally linked to common features such as shear layer lengthening, longer vortex formation length, wavy type flow along the spanwise length of the cylinder, and formation of streamwise and transverse vortices. These flow characteristics are analyzed and discussed in the below sections below.

3.2 The flow patterns of 3D vortex structures

By using the geometry surface modifications as a passive flow control method, the vortex roll-up is delayed and the vortex shedding in the near-wake of cylinders is nearly suppressed. The

instantaneous iso-surfaces of the flow fields in the wake of different cylinders for different λ/D_m at $Re = 3.0\times10^3$ are presented in Fig. 9, 10, and 11. The vortices are rendered by iso-surfaces with Q criterion where $Q = 1$ ($Q = (S_{ij}S_{ji} - e_{ij}e_{ji})/2$, S_{ij} and e_{ji} are vortices and strain rate tensors respectively). The streamwise vortices of the SC cylinder as shown in Fig. 9(a) are visualized as highly three-dimensional and the Karman vortex shedding dominates the wakes in the spanwise direction. The shear layers of the SC cylinder are strongly rolled up and formed vortices near the wake of the cylinder. These vortex structures are suppressed in the wake of wavy cylinders where the free shear layers break down in the wake of cylinders. For SW and DW cylinders, the iso-surfaces have a wavy flow along the spanwise direction which indicates that the free shear layers have a strong 3D effect on the cylinder's surface. As illustrated in Fig. 9(b) and (c), the separated shear layers from the SW and DW cylinders are greatly extended downstream respectively. As a result, the rolling of separated shear layers from the SW and DW cylinders converts into vortices are delayed to downstream which can be observed from Figs. 12 and 13. The vortex shedding behind the wavy cylinders formed further downstream of the cylinders compared to the SC cylinder leading to form longer vortex formation lengths. Additional vortices are formed for SW and DW cylinders and are elongated to downstream compared to SC cylinders. These additional vortices in downstream of the cylinders are broken into several branches as shown in Figs. 12 and 13.

Fig. 10 (a)-(e) shows the instantaneous 3D vortex structures past the SW cylinder for five different wavelength ratios $\lambda/D_m = 3.79 - 6.82$ and constant amplitude ratio $a/D_m = 0.152$. With the increase the λ/D_m, the free shear layer attached to the cylinder increased until $\lambda/D_m = 6.06$ and decreased for $\lambda/D_m = 6.82$. The rolling length of free shear layers increases as the λ/D_m increase downstream of the cylinders. The instantaneous vortex structures of the DW cylinder are presented in Fig. 11 (a)-(e). Similar behavior to SW cylinders is observed for DW cylinders. The vortices generated by SW and DW cylinders are wider in spanwise regions in the wake of cylinders leading to a delay in the vortices roll-up. These vortices of SW and DW cylinders at different λ/D_m stretches downstream and split into several branches. These combining factors lead to high-pressure regions behind the cylinders which support to more drag reduction and suppression in lift fluctuations. These findings on vortical structures of wavy cylinders are consistent with Yoon et al. (2020) and Wei et al. (2016). It can be concluded that the transformation and rolling of vortex patterns are sensitive to λ/D_m and the surface geometry has an influence on the control mechanism of vortex structure patterns of the cylinders.

Fig. 12 and 13 present the streamwise vorticity distributions for SW and DW cylinders, respectively. As the λ/D_m increases up to 6.06, the roll-up of the shear layers into vortices for the wavy cylinders are delayed to downstream of the cylinders. When compared to the SC cylinder, the vortex shedding nearly vanishes in the immediate wake of the SW and DW cylinders and reappears downstream. It can be observed that the vortices formed by the DW cylinder are much closer than those obtained for SW and SC cylinders. Consequently, these vortices spread over the spanwise and streamwise regions leading to stabilizing these vortices which delays the vortices' roll-up.

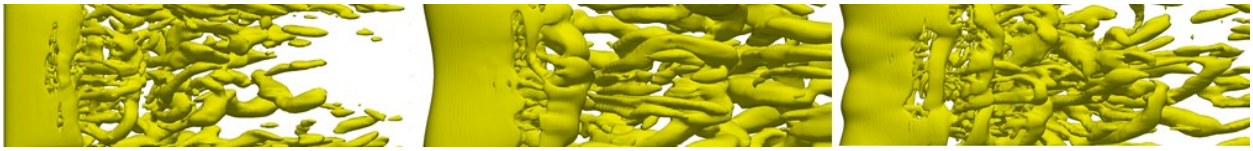

Fig. 9. Iso-surfaces of spanwise vorticity of the shear layer formations (a) SC, (b) SW, and (c) DW at $\lambda/D_m = 6.06$.

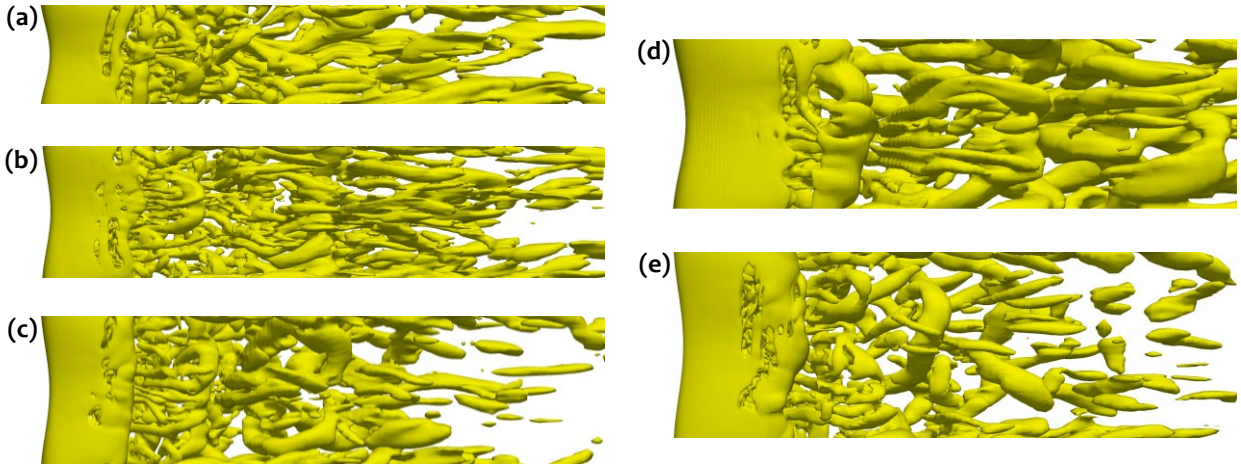

Fig. 10. Iso-surfaces of spanwise vorticity of shear layer formations (a) $\lambda/D_m = 3.79$, (b) $\lambda/D_m = 4.55$, (c) $\lambda/D_m = 5.30$, (d) $\lambda/D_m = 6.06$, and (e) $\lambda/D_m = 6.82$ for SW cylinder.

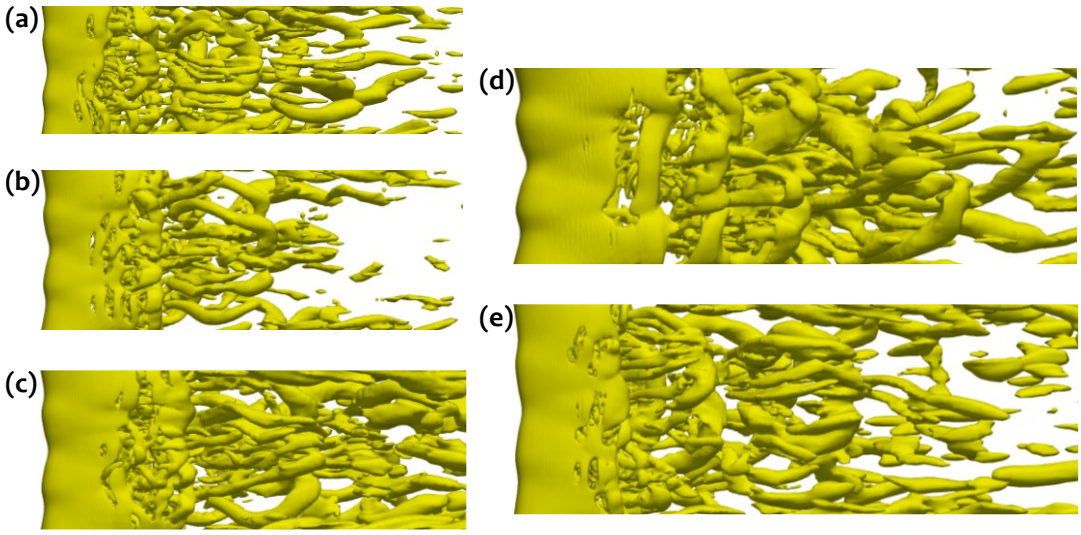

Fig. 11. Iso-surfaces of spanwise vorticity of shear layer formations (a) $\lambda/D_m = 3.79$, (b) $\lambda/D_m = 4.55$, (c) $\lambda/D_m = 5.30$ (d) $\lambda/D_m = 6.06$, (e) $\lambda/D_m = 6.82$ for DW cylinder.

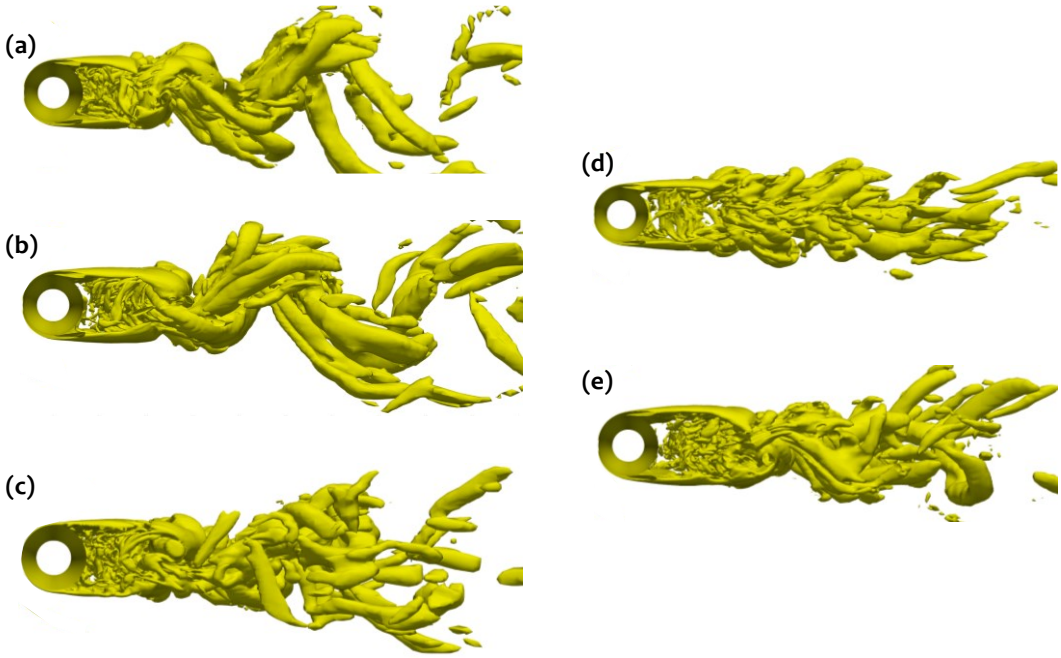

Fig. 12. Instantaneous streamwise vorticity contours in x-y plane (a) $\lambda/D_m = 3.79$, (b) $\lambda/D_m = 4.55$, (c) $\lambda/D_m = 5.30$, (d) $\lambda/D_m = 6.06$, and (e) $\lambda/D_m = 6.82$ for SW cylinder.

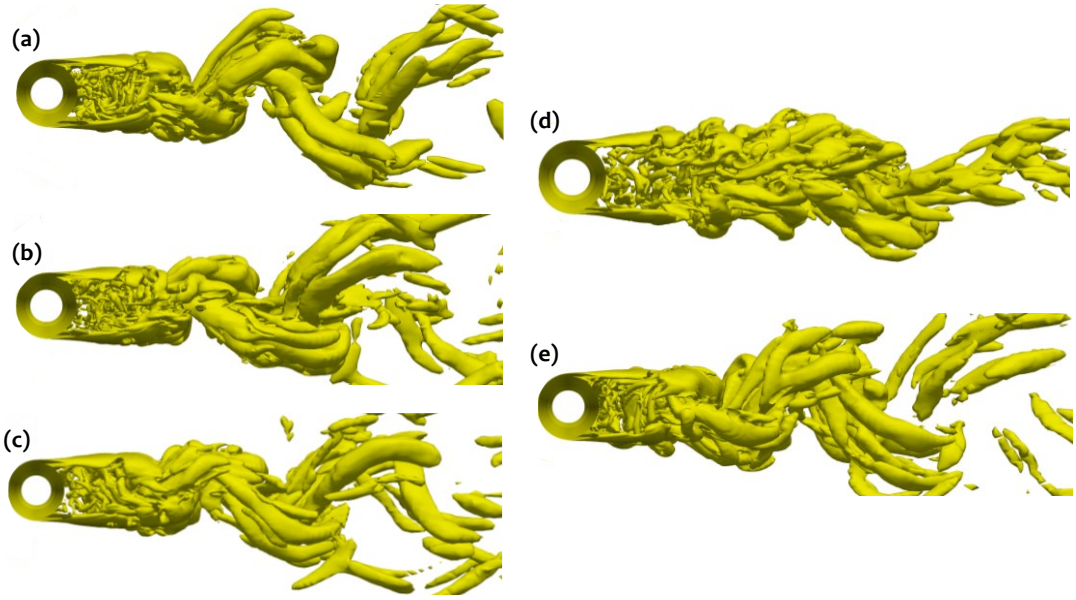

Fig. 13. Instantaneous streamwise vorticity contours in the x-y plane (a) $\lambda/D_m = 3.79$, (b) $\lambda/D_m = 4.55$, (c) $\lambda/D_m = 5.30$, (d) $\lambda/D_m = 6.06$, and (e) $\lambda/D_m = 6.82$ for DW cylinder.

3.3 Vortex formation lengths (L_F)

In the near wake of the cylinder, the vortex formation length (L_F) is linked to the base pressure and hence the drag force (Griffin, 1995). As a result, it is critical to quantify the L_F of the wavy cylinders. Based on Griffin (1995), the time-averaged vortex formation length is defined as the separation between the center of the cylinder and the location where $\bar{u}/U_\infty = 0$ along the centerline of the wake. The stretching of L_F is accomplished by the waviness of the surface as observed from instantaneous spanwise vorticity contours as presented in Fig. 12 and 13. Table 9 presents the L_F of SC, SW, and DW cylinders for five different λ/D_m and $a/D_m = 0.152$ at $Re = 3.0\times10^3$. The L_F increased from nodal plane to saddle plane for both SW and DW cylinders for all λ/D_m. A similar trend was observed in studies by Lee and Nguyen (2007), Lam and Lin (2008), and Zhang et al. (2021). Apparently, L_F of the SW cylinder at every λ/D_m is larger than the SC cylinder. Similarly, L_F of the DW cylinder is longer than the SW and SC cylinders at every λ/D_m. Comparing the L_F for $\lambda/D_m = 3.79-6.82$ for DW cylinder, clearly shows that $\lambda/D_m = 6.06$ has the largest L_F which supports for more drag reduction as shown in Fig. 7. A comparison of variation in L_F for three cylinders is presented in Fig. 14.

Notoriously, in the subcritical flow regime, the $\bar{C}_D$ is directly proportional to negative base pressure ($\bar{C}_{Pb}$). Bearman (1965) highlighted that L_F of SC cylinder was inversely proportional to $\bar{C}_{Pb}$. From these two statements, it can be inferred that as L_F increases, then $\bar{C}_D$ decreases. It can be observed from Table 9, that the DW cylinder with $\lambda/D_m = 6.06$ has the longest L_F, meaning that $\lambda/D_m = 6.06$ should have a small $\bar{C}_D$ value and larger suppression in lift fluctuations compared to other cases studied in this study. This has been confirmed in Section 3.1.

Table 9. Summary of vortex formation length for SC, SW, and DW cylinders.

λ/D_m	Dimensionless vortex formation length (L_F/D_m)				
	SC	SW		DW	
		Node	Saddle	Node 1	Saddle 1
3.79	1.92	2.29	1.87	2.01	2.31
4.55		2.55	2.13	2.36	2.74
5.30		2.92	2.44	2.68	3.23
6.06		3.42	3.15	3.31	3.73
6.82		3.27	3.03	3.25	3.62

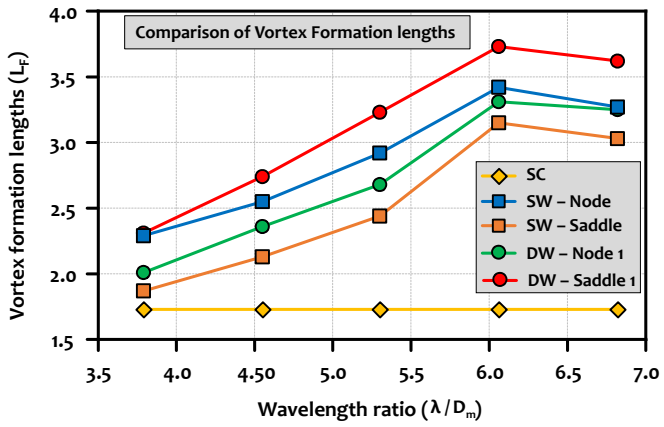

Fig. 14. Comparison of vortex formation lengths for SC, SW, and DW cylinders.

3.4 Flow separation angles

Flow separation angle is a point or line where the boundary layer detaches from the surface of the cylinder and turns into the wake. Shear layer instabilities and the resulting vortex structure features are intimately connected to flow separation characteristics around cylinders. . At this point, the shear stress of the surface vanishes. It is well known that the development of shear layers plays a

vital role in flow control to a reduction in drag and suppression of lift fluctuations. To further comprehend the flow control mechanism, the flow separation angles of cylinders are analyzed.

The variations of separation angles (θ_{sep}) along spanwise direction for SC, SW, and DW cylinder for $\lambda/D_m = 3.79$ to 6.82 from node ($z/\lambda = 0$) to saddle $z/\lambda = 0.50$ are compared as shown in Fig. 15 for $a/D_m = 0.152$ at $Re = 3.0\times10^3$. For wavy cylinders, the separation angles differ from nodal planes to saddle planes. It can be noticed that the θ_{sep} for both SW and DW cylinders are larger than smooth cylinders for all λ/D_m. For both SW and DW cylinders, the separation occurs earlier at saddle points than at the nodal points. This can be attributed due to the wavy fashion of the flow in the wake structure and this kind of phenomenon was observed by Ahmed and Bayes-Muchmore (1992), Zhao et al. (2011), and Lin et al. (2016).

For the SW cylinder, the maximum $\theta_{sep} = 100.4^\circ$ is observed for $\lambda/D_m = 4.55$ at node, while the minimum $\theta_{sep} = 75.2^\circ$ for $\lambda/D_m = 6.82$ at saddle is shown in Fig. 15(a). Conversely, the θ_{sep} for $\lambda/D_m = 6.06$ varies little from the node (93.5°) to saddle (79.6°) compared to other wavelength ratios. Similarly, for DW cylinder, the maximum $\theta_{sep} = 101.4^\circ$ for $\lambda/D_m = 3.79$ at node 1, whereas the minimum $\theta_{sep} = 72.7^\circ$ is observed for $\lambda/D_m = 6.82$ at saddle 2 as shown in Fig. 15(b). Identical to SW cylinder, $\lambda/D_m = 6.06$ showed slight variation in the θ_{sep} between the node and saddle planes for DW cylinder. But the DW cylinder showed a minor variation of θ_{sep} between node and saddle for $\lambda/D_m = 6.06$ when compared to the SW cylinder. Concisely, θ_{sep} at the nodal point is larger than the saddle point for all wavelength ratios. It means that the flow separation at saddle planes occurs earlier than at the nodal planes. This concludes that the optimum $\lambda/D_m = 6.06$ cylinder for SW and DW cylinders produces steadier vortices in the wake of the cylinders, consequently resulting in the longer L_F, reduced $\overline{C}_D$ and $C_{L,RMS}$ as presented in Table 9 and 7 respectively. Comparable results were observed by Lin et al. (2016).

The flow separation lines for three cylinders are shown in Fig. 15 to present the spanwise dependent separation lines for wavy cylinders. To visualize these lines, skin-friction lines for surfaces of the cylinders are generated. In comparison to SC, 3D flow separations were produced by the wavy cylinders. Due to the wavy fashioned surface of the cylinders, the 2D vortex street is deformed and

vortex formations become 3D in the wake of the wavy cylinders. These 3D vortices roll up into an intricate 3D vortex structure father downstream of the cylinder. The stability of free shear layers and wake structures strongly depend on distributions of separation points (Zhao et al., 2011). Notably, the DW cylinder significantly modifies the skin-friction lines when compared to the SW cylinder.

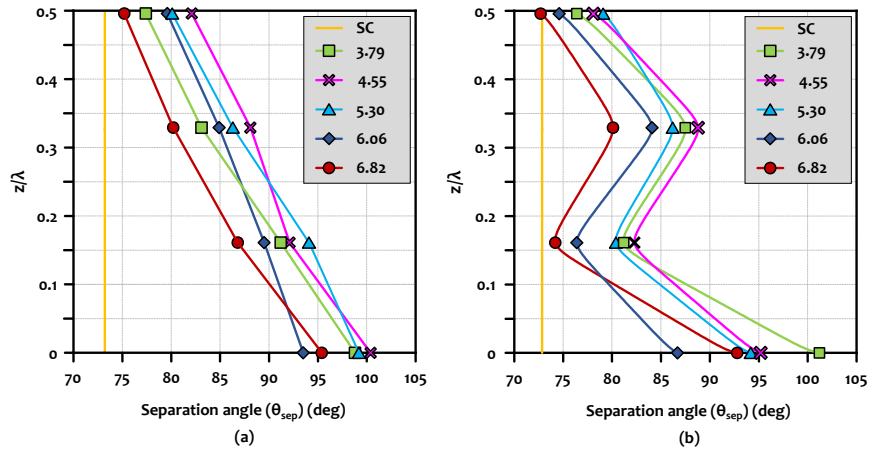

Fig. 15. Comparison of variations in flow separation angles (θ_{sep}) from node - $z/\lambda = 0$ to saddle $z/\lambda = 0.50$ for (a) SW, (b) DW cylinders for $\lambda/D_m = 3.79$ to 6.82 at $Re = 3.0\times10^3$.

3.5 Velocity distributions

The mean streamwise velocity distributions ($\bar{u}/U_\infty$) of SW cylinders at node and saddle are presented in Fig. 16 for $\lambda/D_m = 6.06$ along the centerline of the cylinders (y=0). For comparison purposes, the $\bar{u}/U_\infty$ of previous results from Lin et al. (2016) for SW cylinder and SC from Noberg (1998) are also presented. The $\bar{u}/U_\infty$ of SC cylinder from the present results agrees well with the experimental results by Noberg (1998). For SC cylinder, as x/D_m increases, the $\bar{u}/U_\infty$ decreases until $x/D_m = 1.35$ reaching minimum value and crosses zero at $x/D_m = 1.92$ which is harmonious with Yoon et al. (2017). For the SW cylinder, it can be observed that the present $\bar{u}/U_\infty$ for $\lambda/D_m = 6.06$ at saddle and node matches well with the experimental (Laser Doppler Anemometry - LDA) and numerical (LES) results by Lin et al. (2016). From Fig. 16, it can be concluded that the $\bar{u}/U_\infty$ distributions of SW with $\lambda/D_m = 6.06$ diverging greatly from SC and occur at the father downstream of the cylinder. This implies that the SW cylinder has a larger reversal region than for SC cylinder. Within the SW cylinder, the nodal region demonstrates a larger reversal region than the saddle plane which agrees well with Lin et al. (2016), Yoon et al. (2017), and Jung and Yoon (2014). This confirms that the SW cylinder at

node and saddle plans has longer vortex formation lengths than the smooth circular cylinder which were confirmed as discussed in Section 3.3.

For DW cylinder, Fig. 17 presents the distributions of $\bar{u}/U_\infty$ at node 1, saddle 1, node 2, and saddle 2 planes. Compared to SC and SW cylinders, the minimum value of $\bar{u}/U_\infty$ and crossing the centerline of the cylinder occurred further downstream of the wake of the cylinder for all λ/D_m. It is interesting to note that the DW with saddle plane forms a minimum value of $\bar{u}/U_\infty$ further downstream of the cylinder compared to the nodal plane, which is in contrast to the SW cylinder. As λ/D_m increases, distributions of $\bar{u}/U_\infty$ shifted downstream of the cylinder for nodes 1 and 2, saddle 1 and 2 until $\lambda/D_m = 6.06$ and then increased for $\lambda/D_m = 6.82$. DW cylinder with $\lambda/D_m = 6.06$ has the maximum x/D_m for all nodes and saddle planes when compared to other λ/D_m of DW cylinders, which is consistent with previous observations by Yoon et al. (2020). Whereas $\lambda/D_m = 3.87$ has the minimum x/D_m for all nodal and saddle planes. Interestingly, saddle 1 has the maximum x/D_m, and node 2 has the minimum x/D_m for each λ/D_m, meaning that saddle 1 has the maximum large reversal region while the minimum for node 2 planes. Hence it can be concluded that the variation of $\bar{u}/U_\infty$ strongly depends upon the geometric surface modifications.

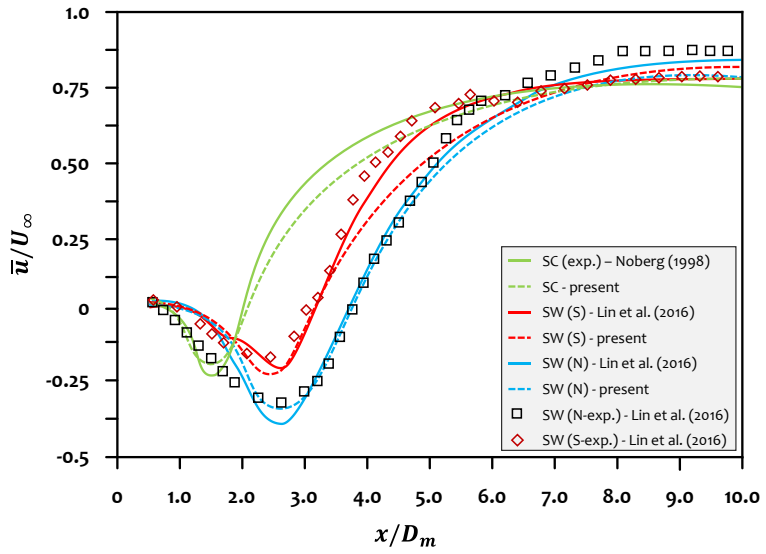

Fig. 16. Mean streamwise velocity distributions ($\bar{u}/U_\infty$) along the centerline of the SC and SW cylinders for $\lambda/D_m = 6.06$ at $Re = 3.0\times10^3$.

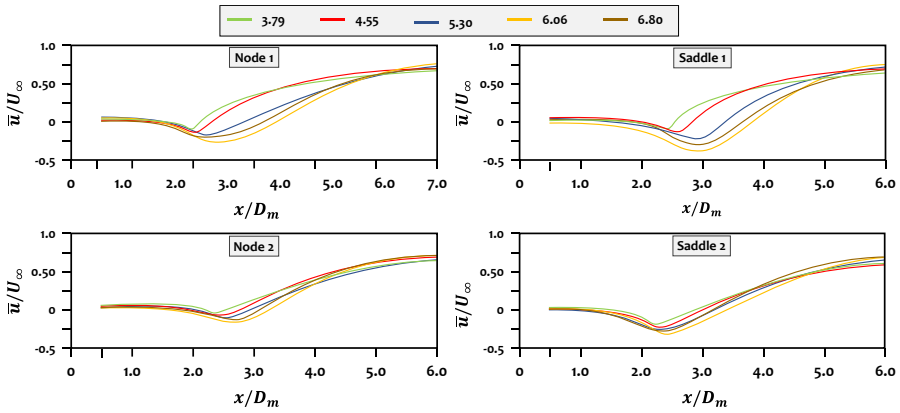

Fig. 17. Mean streamwise velocity distributions ($\bar{u}/U_\infty$) along the centerline of the DW cylinders for $\lambda/D_m = 3.79$ to 6.82 at $Re = 3.0\times10^3$.

3.6 Pressure Coefficients

It is vital to investigate the pressure distribution along the circumference of the cylinders, as $\bar{C}_D$ and $C_{L,RMS}$ are primarily computed from surface pressure at large Re. Fig. 18 and 19 present the variation of streamwise direction mean pressure coefficient ($\bar{C}_P$) for SW and DW cylinders respectively for distinct locations (saddle and nodal planes). The lowest $\bar{C}_P$ for SW and DW cylinders varies along the spanwise direction, meaning that the separation points change along the spanwise direction. The $\bar{C}_P$ for SC cylinder is also presented in Fig. 18 for comparison purposes. It can be noted that $\bar{C}_P$ dramatically diminishes from stagnation point for all three cylinders at different locations and reaches a minimum value (maximum negative) at $\theta \approx 58^\circ - 82^\circ$ and then gradually attained to steady-state after $\theta \approx 90^\circ$.

Compared to SC cylinder, all the locations of SW and DW cylinders have the minimum negative pressure coefficient. Generally, when the wavelength ratio increases, the $\bar{C}_P$ increases. It can be observed that the lowest position of $\bar{C}_P$ at saddle is in front of the nodal planes for SW and DW cylinders, which shows that the separation of flow at saddle planes is earlier than at the nodal planes. The separation angle of cylinders at the saddle plane shifts to a higher angle of flow separation at nodal planes. At $\lambda/D_m = 3.79$, the $\bar{C}_P$ for SW cylinder is almost close to SC cylinder, which suggests that at low λ/D_m, the waviness effect on flow parameters is not evident.

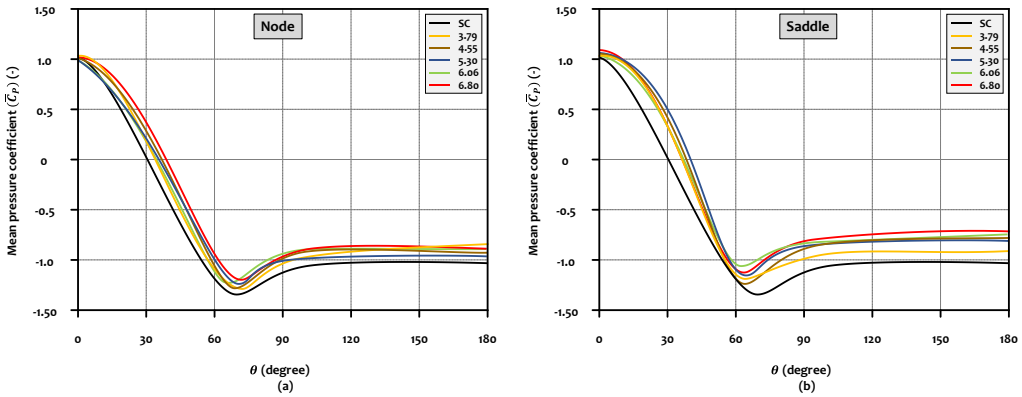

Fig. 18. Variation of mean pressure coefficients ($\bar{C}_P$) (a) Saddle – SW, (b) Node – SW cylinders for different λ/D_m at $Re = 3.9\times10^3$.

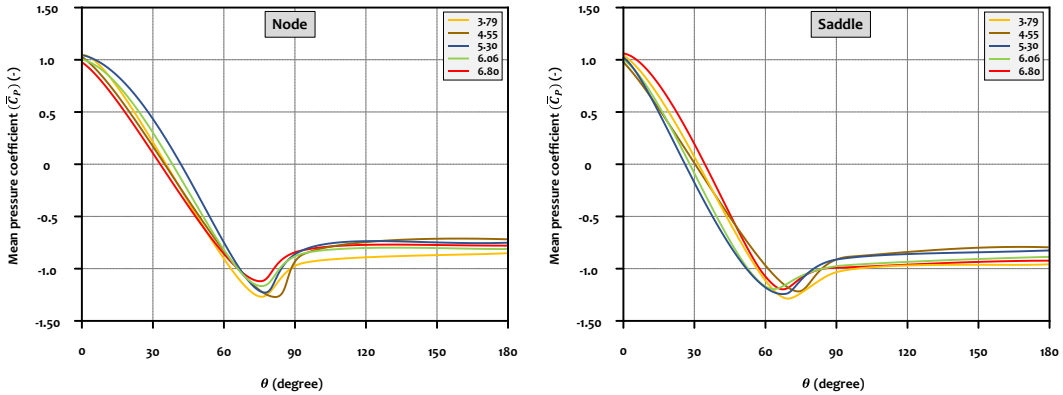

Fig. 19. Variation of mean pressure coefficients ($\bar{C}_P$) (a) Saddle – DW, (b) Node – DW cylinders for different λ/D_m at $Re = 3.9\times10^3$.

4. Concluding remarks

The present study investigated the effect of the waviness of the cylinders on flow characteristics behind the cylinder as a passive flow control method using 3D LES at 3.0×10^3. This study considered $\lambda/D_m = 3.79 - 6.82$ and fixed $a/D_m = 0.152$ to analyze the effect of geometric surface modifications on the flow properties behind the cylinder. The flow characteristics of DW cylinders were compared with SW) and SC cylinders. The difference between the flow control mechanisms of wavy cylinders and smooth circular cylinders can be related to the streamlined distribution of the surfaces of the cylinders in vorticity transportation and deformation. Significant factors that control the flow behind the cylinder are the force exerted by fluid flow over the cylinder. The study concludes as follows:

- At optimal λ/D_m, the SW and DW cylinder attained reductions in $\overline{C}_D$ by 13.49% and 16.69% respectively compared to the SC cylinder.
- Specifically, the $C_{L,RMS}$ of the DW cylinder showed a great decrease of about 94.90% and 63.47% compared to SC and SW cylinders at optimum λ/D_m respectively.
- The reduction in $C_{L,RMS}$ clearly confirms the distribution of pressure on the geometric surface. These features are consistent with longer vortex formation lengths.
- The longer vortex formation length decreased the base pressure coefficient that plays a vital role in influencing the wake forces acting on the cylinder. As the λ/D_m increases, L_F increases until $\lambda/D_m = 6.06$ and then decreases for $\lambda/D_m = 6.82$.
- Consequently, it delays the vortex roll-up and weakens the strength of the vortices. Thus, the drag coefficient and lift fluctuations of wavy cylinders drop dramatically.
- For SW and DW cylinders, the pressure coefficient is different at saddle and nodal planes. The flow separation at saddle planes occurs earlier than at nodal planes for wavy cylinders.
- The pressure component of the drag coefficient control the flow over wavy cylinders.

The flow separation angles and streamwise velocity distributions were also investigated. It is clearly apparent that the flow characteristics and hydrodynamic properties greatly depend upon the geometric surface modifications. The results explained above show why the cylinders with waviness in a spanwise direction with wave amplitude could effectively reduce drag and suppress the lift fluctuations of the cylinders. Hence these kinds of cylinders with waviness are more beneficial in modifying the near-wake structure and controlling the 3D vortices. Even though these kinds of cylinders are rarely used in practical applications, it is concluded by previous researchers and as well as the current investigation that these waviness cylinders have the potential to counter the hydrodynamic forces acting on the structures in fluid flow. However, more studies need to be carried out at high Reynolds numbers, and also with different wave amplitude ratios to study the effect of waviness as a flow control method.

Acknowledgments

This study was conducted through the international collaboration of several institutions. This research was supported by the Brain Pool program funded by the Ministry of Science and ICT through the National Research Foundation of Korea (2021H1D3A2A02094658). The authors also appreciate the

technical support by Dr. Byongug Jeong from the University of Strathclyde (UK), who is supported by the BK21 FOUR Project "2021 Global Visiting Fellow Program" at Seoul National University.

References

Ahn, C.T., Yoon, H.S., Ha, M.Y., Lee, H.G., 2009. Waviness effect of a wavy circular cylinder on the heat transfer at a Reynolds number of 300. International Journal of Heat and Mass Transfer, 52(1-2), 345-354. https://doi.org/10.1016/j.ijheatmasstransfer.2008.05.032.

Assi, G.R., Bearman, P.W., 2018. Vortex-induced vibration of a wavy elliptic cylinder. Journal of Fluids and Structures, 80, 1-21. https://doi.org/10.1016/j.jfluidstructs.2018.02.007.

Assi, G.R., Bearman, P.W., Kitney, N., 2009. Low drag solutions for suppressing vortex-induced vibration of circular cylinders. Journal of Fluids and Structures, 25(4), 666-675. https://doi.org/10.1016/j. jfluidstructs.2008.11.002.

Bai, H.L., Alam, M.M., Gao, N., Lin, Y.F., 2019. The near wake of sinusoidal wavy cylinders: three-dimensional POD analyses. International Journal of Heat and Fluid Flow, 75, 256-277. https://doi.org/10.1016/j. ijheatfluidflow.2019.01.013.

Bearman, P.W., 1965. Investigation of the flow behind a two-dimensional model with a blunt trailing edge and fitted with splitter plates. Journal of fluid mechanics, 21(2), 241-255. https://doi.org/10.1017/ S0022112065000162.

Bearman, P., Branković, M., 2004. Experimental studies of passive control of vortex-induced vibration. European Journal of Mechanics-B/Fluids, 23(1), 9-15. https://doi.org/10.1016/j.euromechflu.2003.06.002.

Bearman, P.W., Owen, J.C., 1998. Reduction of bluff-body drag and suppression of vortex shedding by the introduction of wavy separation lines. Journal of Fluids and Structures, 12(1), 123-130. https://doi.org/ 10.1006/jfls.1997.0128.

Choi, H., Jeon, W.P., Kim, J., 2008. Control of flow over a bluff body. Annu. Rev. Fluid Mech., 40, 113-139. https://doi.org/10.1146/annurev.fluid.39.050905.110149.

Darekar, R.M., Sherwin, S.J., 2001. Flow past a square-section cylinder with a wavy stagnation face. Journal of Fluid Mechanics, 426, 263-295. https://doi.org/10.1017/S0022112000002299.

Deardorff, J.W., 1970. A numerical study of three-dimensional turbulent channel flow at large Reynolds numbers. Journal of Fluid Mechanics, 41(2), 453-480. https://doi.org/10.1017/ S0022112070 000691.

Dong, S., Karniadakis, G.E., Ekmekci, A., Rockwell, D., 2006. A combined direct numerical simulation–particle image velocimetry study of the turbulent near wake. Journal of Fluid Mechanics, 569, pp.185-207. https://doi.org/10.1017/S0022112006002606.

Germano, M., Piomelli, U., Moin, P., Cabot, W.H., 1991. A dynamic subgrid-scale eddy viscosity model. Physics of Fluids A: Fluid Dynamics, 3(7), 1760-1765. https://doi.org/10.1063/1.857955.

Griffin, O.M., 1995. A note on bluff body vortex formation. Journal of Fluid mechanics, 284, pp.217-224. https://doi.org/10.1017/S0022112095000322.

Jie, H., Liu, Y.Z., 2017. Large eddy simulation and proper orthogonality decomposition of turbulent flow around a vibrissa-shaped cylinder. International Journal of Heat and Fluid Flow, 67, 261-277. https://doi.org/10.1016/j.ijheatfluidflow.2017.09.001.

Jung, J.H., Yoon, H.S., 2014. Large-eddy simulation of flow over a twisted cylinder at a subcritical Reynolds number. Journal of fluid mechanics, 759, 579-611. https://doi.org/10.1017/jfm.2014.581.

Kravchenko, A.G., Moin, P., 2000. Numerical studies of flow over a circular cylinder at Re D= 3900. Physics of fluids, 12(2), pp.403-417. https://doi.org/10.1063/1.870318.

Lam, K., Lin, Y.F., 2008. Large-eddy simulation of flow around wavy cylinders at a subcritical Reynolds number. International Journal of Heat and Fluid Flow, 29(4), 1071-1088. https://doi.org/10.1016/j.ijheatfluidflow.2008.01.006.

Lam, K., Lin, Y.F., 2009. Effects of wavelength and amplitude of a wavy cylinder in cross-flow at low Reynolds numbers. Journal of Fluid Mechanics, 620, 195-220. https://doi.org/10.1017/S0022112008004217.

Lam, K., Wang, F.H., Li, J.Y., So, R.M.C., 2004a. Experimental investigation of the mean and fluctuating forces of wavy (varicose) cylinders in a cross-flow. Journal of fluids and structures, 19(3), 321-334. https://doi.org/10.1016/j.jfluidstructs.2003.12.010.

Lam, K., Wang, F.H., So, R.M.C., 2004b. Three-dimensional nature of vortices in the near wake of a wavy cylinder. Journal of fluids and structures, 19(6), 815-833. https://doi.org/10.1016/j.jfluidstructs.2004.04.004.

Lee, S.J., Nguyen, A.T., 2007. Experimental investigation on wake behind a wavy cylinder having sinusoidal cross-sectional area variation. Fluid dynamics research, 39(4), 292. https://doi.org/10.1016 /j.fluiddyn.2006.06.003.

Lekkala, M.R., Latheef, M., Jung, J.H., Coraddu, A., Zhu, H., Srinil, N., Lee, B.H. and Kim, D.K., Recent advances in understanding the flow over bluff bodies with different geometries at moderate Reynolds numbers. http://dx.doi.org/10.1016/j.oceaneng.2022.111611.

Lin, Y.F., Bai, H.L., Alam, M.M., Zhang, W.G., Lam, K., 2016. Effects of large spanwise wavelength on the wake of a sinusoidal wavy cylinder. Journal of fluids and structures, 61, 392-409. https://doi.org/10. 1016/j.jfluidstructs.2015.12.004.

Lu, X., Dalton, C., Zhang, J., 1997. Application of large eddy simulation to flow past a circular cylinder. https://doi.org/10.1115/1.2829099.

Moon, J., Yoon, H.S., Kim, H.J., Kim, M.I., 2019. Forced convection heat transfer from an asymmetric wavy cylinder at a subcritical Reynolds number. International Journal of Heat and Mass Transfer, 129, 707-720. https://doi.org/10.1016/j.ijheatmasstransfer.2018.10.029.

Nam, S.H., Yoon, H.S., 2022. Effect of the wavy geometric disturbance on the flow over elliptic cylinders with different aspect ratios. Ocean Engineering, 243, 110287. https://doi.org/10.1016/j.oceaneng.2021.110287.

Naudascher, E., Rockwell, D., 2005. Flow-induced vibrations: an engineering guide. Routledge.

New, T.H., Shi, S., Liu, Y., 2013. Cylinder-wall interference effects on finite-length wavy cylinders at subcritical Reynolds number flows. Experiments in fluids, 54(10), 1-24. https://doi.org/10.1007/s00348-013-1601-8.

Norberg, C., 1988. Effects of Reynolds number and a low-intensity freestream turbulence on the flow around a circular cylinder. Chalmers University, Goteborg, Sweden, Technological Publications, 87(2), 1-55.

Owen, J.C., Bearman, P.W., Szewczyk, A.A., 2001. Passive control of VIV with drag reduction. Journal of Fluids and Structures, 15(3-4), 597-605. https://doi.org/10.1006/jfls.2000.0358.

Smagorinsky, J., 1963. General circulation experiments with the primitive equations: I. The basic experiment. Monthly weather review, 91(3), 99-164. https://doi.org/10.1175/1520-0493(1963)091%3C0099:GCEWTP%3E2.3.CO;2.

Sohankar, A., Khodadadi, M., Rangraz, E., Alam, M.M., 2019. Control of flow and heat transfer over two inline square cylinders. Physics of Fluids, 31(12), 123604. https://doi.org/10.1063/1.5128751.

Xu, C.Y., Chen, L.W., Lu, X.Y., 2010. Large-eddy simulation of the compressible flow past a wavy cylinder. Journal of Fluid Mechanics, 665, pp.238-273. https://doi.org/10.1017/S0022112010003927.

Xu, C.Y., Zhang, Y.T., Hou, B., Sun, J.H., 2019. Numerical investigations of the compressible turbulent flow past wavy-axis cylinder. Fluid Dynamics Research, 51(5), 055502. https://doi.org/10.1088/1873-7005/ ab2f84.

Yoon, H.S., Balachandar, S., Ha, M.Y., 2009. Large-eddy simulation of flow in an unbaffled stirred tank for different Reynolds numbers. Physics of fluids, 21(8), 085102. https://doi.org/10.1063/ 1.3210776.

Yoon, H.S., Kim, H.J., Wei, D.J., 2018. Forced convection heat transfer from the helically twisted elliptic cylinder inspired by a daffodil stem. International Journal of Heat and Mass Transfer, 119, 105-116. https://doi.org/10.1016/j.ijheatmasstransfer.2017.11.107.

Yoon, H.S., Oh, K.J., Kim, H.J., Kim, M.I., Moon, J., 2020. Double wavy geometric disturbance to the bluff body flow at a subcritical Reynolds number. Ocean Engineering, 195, 106713. https://doi.org/10.1016/j.oceaneng.2019.106713.

Yoon, H.S., Shin, H., Kim, H., 2017. Asymmetric disturbance effect on the flow over a wavy cylinder at a subcritical Reynolds number. Physics of Fluids, 29(9), 095102. https://doi.org/10.1063 /1.5001968.

Zhang, K., Katsuchi, H., Zhou, D., Yamada, H., Bao, Y., Han, Z., Zhu, H., 2018. Numerical study of flow past a transversely oscillating wavy cylinder at Re= 5000. Ocean Engineering, 169, pp.539-550. https://doi.org/10.1016/j.oceaneng.2018.09.006.

Zhang, W., Lee, S.J., 2005. PIV measurements of the near-wake behind a sinusoidal cylinder. Experiments in fluids, 38(6), 824-832. https://doi.org/10.1007/s00348-005-0981-9.

Zhang, Z., Tu, J., Zhang, K., Yang, H., Han, Z., Zhou, D., Xu, J., Zhang, M., 2021. Vortex characteristics and flow-induced forces of the wavy cylinder at a subcritical Reynolds number. Ocean Engineering, 222, 108593. https://doi.org/10.1016/j.oceaneng.2021.108593.

Zhao, R., Xu, J.L., Yan, C., Yu, J., 2011. Scale-adaptive simulation of flow past wavy cylinders at a subcritical Reynolds number. Acta Mechanica Sinica, 27(5), pp.660-667. https://doi.org/10.1007/s10409-011-0490-4.

Zheng, H., Wang, J., 2021. A numerical study on the flow-induced vibrations of flexible cylinders attached with fixed short fairings. Ocean Engineering, 229, 108904. https://doi.org/10.1016/j.oceaneng.20 21.108904.

Zhou, T., Razali, S.M., Hao, Z., Cheng, L., 2011. On the study of vortex-induced vibration of a cylinder with helical strakes. Journal of Fluids and Structures, 27(7), 903-917. https://doi.org/10.1016/j.jfluidstructs.2011.04.014.

Zhuang, Y.Q., Sun, X.J., Huang, D.G., 2018. Numerical study of unsteady flows past a rotating wavy cylinder. European Journal of Mechanics-B/Fluids, 72, 538-544. https://doi.org/10.1016/j.euromechflu. 2018.07.017.

Nomenclature	
a	The amplitude of waviness of the cylinder
C_D	Drag coefficient
C_L	Lift coefficient
$\overline{C}_D$	Mean drag coefficient
$C_{L,RMS}$	Root mean square of lift coefficient
D_m	Mean diameter of the cylinder
D_{min}	Minimum diameter of the cylinder
D_{max}	Maximum diameter of the cylinder
f_s	Vortex shedding frequency
L_f	Vortex formation length
p	pressure
St	Strouhal number
t	Time
Re	Reynolds number
u_i	Velocity in 'i^{th}' direction
U_∞	Free stream velocity of the flow
x_i	Cartesian coordinates
λ	The wavelength of the waviness of the cylinder
ν	Kinematic viscosity
ρ	The density of the fluid
Pr	Prandtl number
RMS	Root mean square